




OPEN

Design and analysis of centrifugal compressor in carbon dioxide heat pump system

Peng Jiang , Yong Tian, Bo Wang & Chaohong Guo

Based on the advantages of energy saving, environmental protection and high efficiency, carbon dioxide heat pump system has great application prospects. However, there are still many technical problems to be solved, especially the design and optimization of carbon dioxide centrifugal compressor. In this paper, a centrifugal compressor in carbon dioxide heat pump system is designed. The compressor is directly driven by a high-speed permanent magnet synchronous motor. Two-stage impellers are installed on both sides of the motor, and the bearings are active magnetic bearings. The influences of inlet pressure and temperature on compressor performance are analyzed. In the range of inlet temperature from 35 to 55 °C, with the decrease of inlet temperature, the compressor pressure ratio increases by 12–29.8%, the power increases by 2.7–8.6%. In the range of inlet pressure from 4 to 6 MPa, with the increase of inlet pressure, the compressor pressure ratio increases by 12.3–38.6%, and the power increases by 8.7–17.8%. In addition, the calculation method of compressor axial force is introduced, the axial force is calculated, analyzed and optimized. Furthermore, the rotor dynamics of compressor rotor and the influences of bearing stiffness and diameter of motor rotor on rotor dynamics are studied. With the increase of bearing stiffness, the first-order critical speed and maximum displacement of the rotor increase. The research provides a theoretical reference for the design and optimization of centrifugal compressor in carbon dioxide heat pump system.

Keywords Carbon dioxide heat pump, Carbon dioxide centrifugal compressor, Compressor performance, Axial force, Rotor dynamics

List of symbols

P_0	Inlet total pressure of compressor (MPa)
p_0	Pressure in front of the impeller inlet hub (MPa)
p_1	Inlet pressure of impeller (MPa)
p_2	Outlet pressure of impeller (MPa)
n	Impeller rotating speed (r/min)
F_1	Axial force acting on the inlet face of impeller (kN)
F_2	Axial force acting on the inlet–outlet part of impeller (kN)
F_{1m}	Axial force generated by the change of momentum from axial direction to radial direction (kN)
r_1	Radius of impeller inlet (m)
d_m	Diameter of the sealing diameter between the back of the impeller and the motor (m)
D_1	Diameter of impeller inlet (m)
K_{xx}/K_{yy}	Stiffness of the journal bearing (N/mm)
F_{tot1}	Axial force of first-stage impeller (kN)
d_{m1}	Diameter of the sealing diameter between the back of the first-stage impeller and the motor (m)
d_r	Diameter of motor rotor (mm)
T_0	Inlet total temperature of compressor (°C)
F_{tot}	Axial force of compressor (kN)
C_{01}	Inlet velocity (m/s)
Q_m	Mass Flow Rate (kg/s)
D_0	Diameter of impeller inlet hub (m)
F_0	Axial force acting on the inlet hub of impeller (kN)
F_3	Axial force acting on the impeller back (kN)

Institute of Engineering Thermophysics, Chinese Academy of Sciences, 11 North Fourth Ring West Road, Beijing 100190, People's Republic of China. ✉ email: jiangpeng@iet.cn

F_{10}	Axial force generated by the static pressure of inlet gas (kN)
r_2	Radius of impeller outlet (m)
$F_{\text{tot}1,2}$	Axial force of the first-stage impeller or the second-stage impeller (kN)
D_2	Diameter of impeller outlet (m)
C_{xx}/C_{yy}	Damping of the journal bearing (N-s/mm)
$F_{\text{tot}2}$	Axial force of second-stage impeller (kN)
d_{m2}	Diameter of the sealing diameter between the back of the second-stage impeller and the motor (m)

With the development of social economy, human demand for energy continues to increase, and fossil energy still accounts for more than 80% of global energy consumption, which has caused a series of environmental problems. Therefore, it is urgent to find alternative clean and renewable energy^{1,2}. In recent years, the utilization modes of new energy sources such as nuclear energy^{3,4}, solar energy^{5,6}, wind energy^{7,8}, biomass energy^{9,10}, hydrogen energy^{11,12}, geothermal energy¹³ and tidal energy¹⁴ have been deeply studied.

Similarly, improving energy efficiency is also an important means to save energy and reduce emissions. Through the heat pump effect, the energy of low-temperature heat source can be effectively utilized and the system efficiency can be improved. Natural refrigerants widely used in heat pump systems include carbon dioxide, ammonia, butane, isobutane and propylene¹⁵. The ozone depletion potential of carbon dioxide is zero, and it is neither explosive nor toxic, and it is cheap, which makes the carbon dioxide heat pump system widely studied^{16–22}. Xu et al.¹⁸ put forward an improved integrated CO₂ heat pump system, which can improve thermal comfort and reduce economic cost, and can operate in hot water combined mode and space heating mode. Nawaz et al.¹⁹ developed a performance model to evaluate the characteristics of a transcritical CO₂ HPWH system, and found that the set value of water supply temperature has a great influence on the system performance. A new pumped thermal energy storage (PTES) structure with supercritical CO₂ as working fluid and molten salt as heat storage fluid was proposed by Tafur-Escant et al.²⁰, and the net power generated by this novel proposal is 12.46 MW in load and 10 MW in discharge, achieving an efficiency of 80.26%. Qin et al.²¹ put forward a new compression/injection transcritical CO₂ heat pump system for simultaneous cooling and heating, and found that the new system has 12% higher efficiency than the injection system, and produces the shortest payback period of 1.10 years among the three systems considered. Wang et al.²² conducted experimental research on the hot gas bypass defrosting method and found that, except for the initial stage, the measured parameters gradually change during the defrosting process, and the defrosting time is within the specified defrosting range.

As the core component of heat pump system, compressor plays an important role in system efficiency. At present, the main types of compressors used for carbon dioxide are piston compressor^{23,24}, scroll compressor^{25,26}, screw compressor²⁷ and centrifugal compressor²⁸. In recent years, a lot of research work has been done to improve the performance of carbon dioxide compressor. A model of the thermal compressor was developed and validated by Ibsaine et al.²³. The simulation results related to the regenerator, piston rod diameter, adiabatic dead volume size, and working fluid leakage in the annular gap between the cylinder liner and piston are provided. Zheng et al.^{25,26} proposed a passive flow control method for the radial leakage problem of vortex compressors using micro grooves at the end of the vortex envelope and continuous sealing grooves on the static vortex sidewall. They conducted numerical research on their flow characteristics and found that the aerodynamic and thermodynamic performance of oil-free vortex compressors can be effectively improved by using micro groove vortex blade tips under reasonable working conditions and micro groove geometry. How the rotor force generated by compression and expansion processes is partially balanced to reduce radial bearing force and eliminate axial force was demonstrated by Stosic et al.²⁷.

Centrifugal compressor has the advantages of small volume, light weight and compact structure. The design method, performance and application effect in carbon dioxide cycle have also been studied by scientists^{28–33}. A mean line model for centrifugal compressors and a coupling optimization method with heat pump systems, and coupled and optimized the compressor model with a heat pump cycle model supplying steam at 150 °C are proposed by Meroni et al.²⁸. Cao et al.²⁹ proposed a design strategy to improve the aerodynamic performance of supercritical CO₂ centrifugal compressors and suppress condensation, and found that increasing the inlet compression coefficient or density within the studied operating conditions would reduce the condensation area. A 150 kW supercritical CO₂ centrifugal compressor for a 500 kW power generation system was designed and studied by Park et al.³⁰. The design point, pressure ratio, and efficiency of the compressor are 1.75 and 80%, respectively, with a speed of 36000 RPM. Hosseinpour et al.³¹ designed a single stage s-CO₂ centrifugal impeller for simple recovery of s-CO₂ in the Brayton cycle. A new set of design guidelines for s-CO₂ compressors from zero-dimensional, one-dimensional, and three-dimensional perspectives were proposed by Xu et al.³². Xia et al.³³ proposed and simulated a simple regeneration cycle of 5 MW s-CO₂ for a small lead cooled fast reactor (SLFR) for the first time, and designed an s-CO₂ compressor for this cycle.

At present, there is little research on the design and application of centrifugal compressor in carbon dioxide heat pump, especially the centrifugal compressor with magnetic bearings and permanent magnet synchronous motor, which has the advantages of compact structure, oil-free, non-leakage and high efficiency. Because of the high working pressure of carbon dioxide heat pump, centrifugal compressor, as the core component of heat pump, puts forward higher requirements for its axial force optimization. In this study, the axial force of the whole machine is optimized to control it in a reasonable range. At the same time, the compressor structure (CMC structure) which directly drives one impeller on both sides of the high-speed motor is adopted in this study, which increases the length of the motor rotor, which poses a greater challenge to the check of rotor dynamics. Therefore, the design and optimization of compressor in this study are of great significance to the popularization and use of carbon dioxide heat pump.

The carbon dioxide heat pump system is built in Lianyungang City, Jiangsu Province, as an auxiliary system of High-Efficiency Low-Carbon Gas Turbine Test Device, which is mainly used for waste heat recovery in hot water. The schematic diagram of carbon dioxide heat pump system is shown in Fig. 1. The temperature of the low temperature heat source is 40 °C, the heating capacity of the system is greater than 1 MW, and the external water supply temperature is higher than 70 °C. This article introduces the preliminary design of single-shaft back-to-back CO₂ centrifugal compressor used in CO₂ heat pump system, introduces the calculation and optimization method of axial force of CO₂ centrifugal compressor, and analyzes the influences of magnetic bearing stiffness and diameter of motor rotor on rotor dynamics.

Rotor layout

The layout of the carbon dioxide compressor is shown in Fig. 2, and the descriptions of each component are as follows.

- (1) Nut
- (2) First Stage Impeller
- (3) Seal Structure
- (4) Thrust Collar
- (5) Thrust Bearing
- (6) Motor Stator
- (7) Motor Rotor
- (8) Radial Bearing
- (9) Second Stage Impeller

The carbon dioxide centrifugal compressor will be designed according to API 617³⁴. Nuts are used to fix the rotor in the axial direction, and the impeller and the motor cavity are sealed by a sealing structure. The motor adopts a permanent magnet synchronous motor, and the compressor impeller is installed on both sides of the motor shaft and directly driven by the motor. Comb seal or dry gas seal can be selected as the sealing structure according to the design requirements. Both the radial bearing and the thrust bearing adopt active magnetic suspension bearings, which have long service life and do not need a lubricating oil system. Most axial force can be offset by the back-to-back design of the first-stage impeller and the second-stage impeller, and the balance of residual axial force in the whole rotor system is finally realized by the thrust bearing.

Compressor sizing

According to the conditions of carbon dioxide heat pump cycle, the operating conditions of the compressor are determined as shown in Table 1. The aerodynamic design of compressor is completed using Compal software³⁵. The first-stage design pressure ratio is 1.6, and the second-stage design pressure ratio is 1.43. The parameters of the two-stage impellers are shown in Table 2.

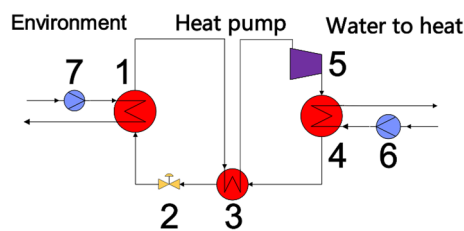


Figure 1. Schematic diagram of carbon dioxide heat pump system. 1, 3, 4. Heat exchanger; 2. Control valve; 5. Compressor; 6, 7. Pump.

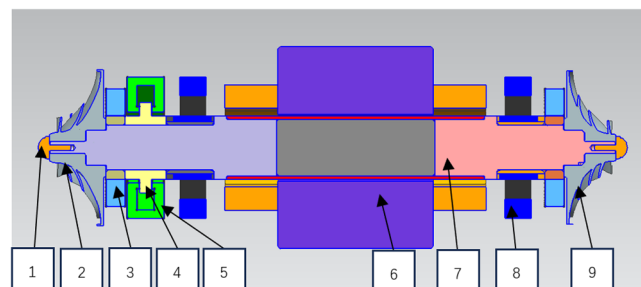


Figure 2. Layout of carbon dioxide compressor.

Parameter	Compressor
Inlet pressure P_1 /MPa	4.95
Inlet temperature T_1 /°C	45
Inlet mass flow rate/kg s^{-1}	≥ 6
Outlet pressure P_2 /MPa	11
Max speed/rpm	26000

Table 1. Operating conditions for compressor design.

Parameter	First stage	Second stage
Impeller-hub inlet diameter/mm	26.0	23.2
Impeller exit diameter/mm	133	130.3
Impeller exit width/mm	3.93	3.64
Clearance gap/mm	0.3	0.3
Number of impeller main blades	7	7
Number of impeller splitter blades	7	7
Vaneless diffuser exit diameter/mm	172.9	169.4

Table 2. Parameters of impellers.

The three-phase distribution diagram of carbon dioxide is shown in Fig. 3, and the Inlet state of compressor (point 1) and outlet state (point 2) are identified in Fig. 3. Carbon dioxide at the inlet of the compressor is in a gaseous state, and the carbon dioxide at the outlet after being compressed by the impellers is in supercritical state, so the whole compression process is transcritical.

The layout of the two-stage centrifugation compressor design is shown in Fig. 4. A diffuser and a volute are designed behind each stage impeller, and the outlet of the first stage volute is connected with the inlet of the second stage impeller through an external pipeline.

The performance of compressor can be accurately predicted by Compal software. The performance curves of the compressor are shown in Fig. 5. With the increase of flow rate, the pressure ratio of compressor decreases, the power increases, and the efficiency first increases and then decreases. With the increase of rotating speed, the pressure ratio and power of the compressor gradually increase. At low speed, the efficiency of compressor changes more sharply with the flow rate. The main reason is that the working point deviates greatly from the rated design point when the compressor is running at low speed.

Because carbon dioxide is gaseous at the compressor inlet, as shown in Fig. 6, the density of carbon dioxide is greatly influenced by temperature and pressure. When the temperature is 45 °C and the pressure increases from 4 to 6 MPa, the density of carbon dioxide increases by 74.4%. The density of carbon dioxide increased by 20.5% when the pressure was 4.95 MPa and the temperature was increased from 30 to 60 °C. In the carbon dioxide heat pump cycle, the inlet parameters will also change with the external parameters when the compressor is running, so it is of great significance to study the influence of compressor inlet parameters on compressor performance for compressor control in the cycle.

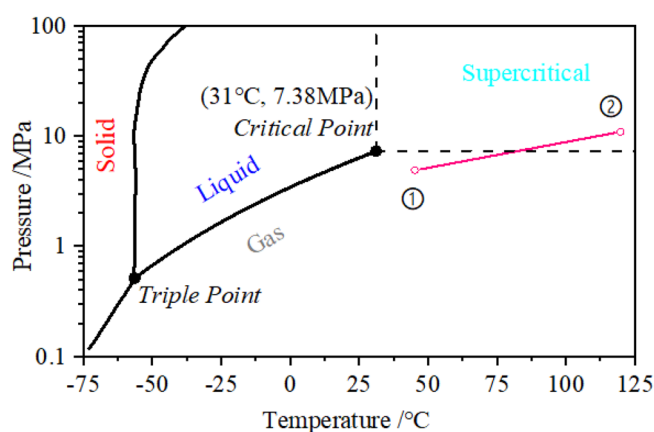


Figure 3. Carbon dioxide three-phase distribution diagram.

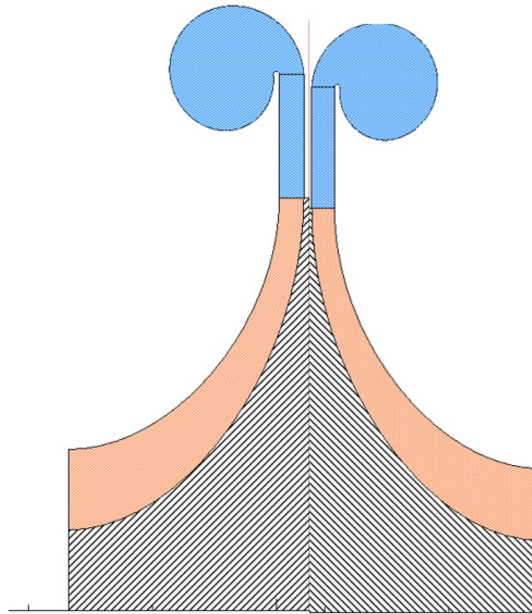


Figure 4. Layout of the Two-Stage Compressor Design.

The predicted performance curves of the compressor at 26000 rpm, inlet pressure of 4.95 MPa and inlet temperature from 35 to 55 °C are shown in Fig. 7. In the range of inlet temperature from 35 to 55 °C, with the decrease of inlet temperature, the compressor pressure ratio increases by 12–29.8%, the power increases by 2.7–8.6%, and the efficiency decreases more slowly after the design point. This is mainly because, at the same inlet pressure, with the decrease of temperature, the density of carbon dioxide increases, and the volume flow at the inlet of the compressor decreases, so that a larger pressure ratio can be achieved at the same speed, and similarly, the compressor power will also increase.

The predicted performance curves of the compressor at 26000 rpm, inlet temperature of 45 °C and inlet pressure from 4 to 6 MPa are shown in Fig. 8. In the range of inlet pressure from 4 to 6 MPa, with the increase of inlet pressure, the compressor pressure ratio increases by 12.3–38.6%, and the power increases by 8.7–17.8%. The maximum inlet mass flow of compressor at inlet pressure of 4 MPa is 21.4% lower than that at inlet pressure of 6 MPa. With the increase of pressure, the density of carbon dioxide increases, the volume flow at the inlet of compressor decreases and the pressure ratio increases. When the inlet pressure of the compressor is 6 MPa, the pressure ratio of the compressor changes relatively little with the flow rate, mainly because the higher the inlet pressure, the greater the carbon dioxide density, and the smaller the change of the inlet volume flow rate in the same mass flow range.

Axial force analysis

The centrifugal compressor in carbon dioxide heat pump cycle has high pressure and high density, which leads to a very large axial force of a single impeller and requires high design requirements for axial thrust bearings. Therefore, it is necessary to accurately predict and optimize the axial force of the compressor to ensure its safe and stable operation. The axial force of carbon dioxide compressor is related to many parameters, such as flow rate, sealing diameter, impeller size, impeller inlet and outlet pressure, temperature and so on. In the design process of carbon dioxide compressor, the calculation method of axial force of compressor is as follows.

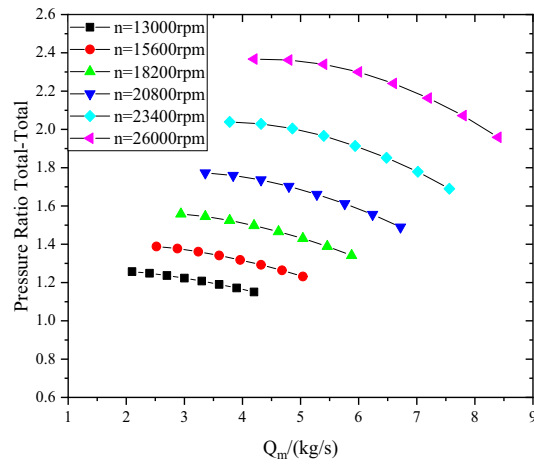
As shown in Fig. 2, the two-stage impellers of the compressor designed in this study are set back to back, and the axial force directions of the two impellers are opposite, and the axial force of the compressor is as shown in Eq. (1). As shown in Fig. 9, the axial force of the single-stage impeller of the compressor is mainly divided into four parts. The gas force F_0 acts on the inlet hub of the compressor impeller, the gas force F_1 acts on the inlet surface, the gas force F_2 acts on the inlet–outlet part of the impeller, and the gas force F_3 acts on the back part of the impeller from the sealing diameter to the outer diameter of the impeller. The relationship between the parts is as follows.

$$F_{tot} = F_{tot1} - F_{tot2} \quad (1)$$

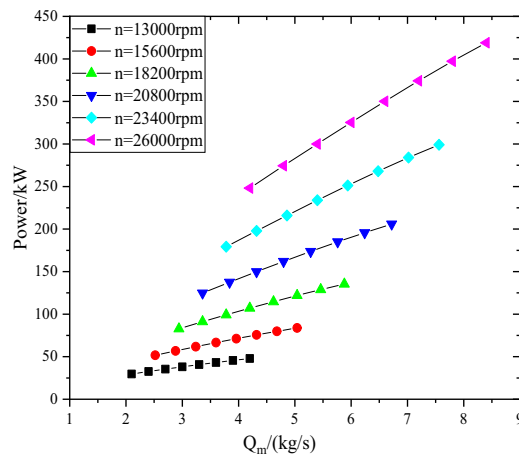
$$F_{tot1,2} = F_3 - F_2 - F_1 - F_0 \quad (2)$$

$$F_0 = \frac{\pi}{4} D_0^2 p_0 \quad (3)$$

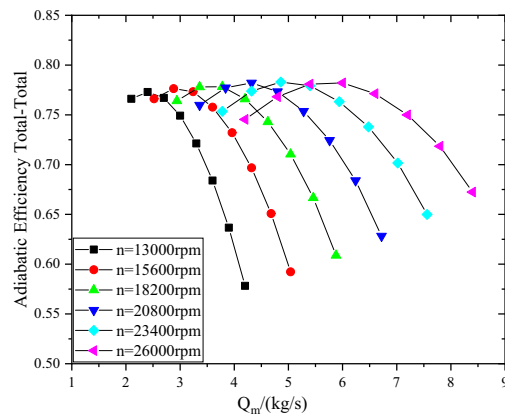
$$F_1 = F_{10} + F_{1m} \quad (4)$$



(a) Pressure ratio total-total versus Q_m



(b) Power versus Q_m



(c) Adiabatic efficiency total-total versus Q_m

Figure 5. Performance curves of the compressor at 13000–26000 rpm.

where F_{tot} is the axial force of compressor, F_{tot1} is the axial force of first-stage impeller, F_{tot2} is the axial force of second-stage impeller, $F_{tot1,2}$ is the axial force of the first-stage impeller or the second-stage impeller, D_0 is the diameter of the impeller inlet hub, and p_0 is the pressure in front of the impeller inlet hub. Where F_{10} is the axial force generated by the static pressure of inlet gas, and F_{1m} is the axial force generated by the change of momentum from axial direction to radial direction³⁶. The calculation formulas are as follows:

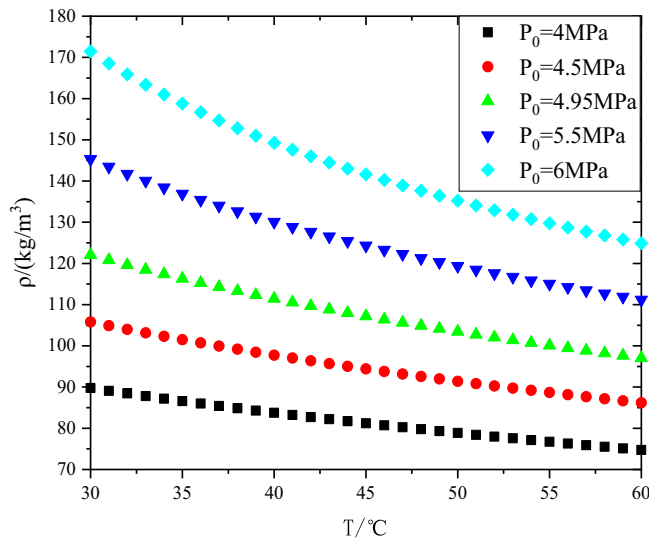


Figure 6. Variation diagram of carbon dioxide density with temperature and pressure.

$$F_{10} = \frac{\pi(D_1^2 - D_0^2)}{4} p_1 \tag{5}$$

$$F_{1m} = Q_m c_{01} \tag{6}$$

$$F_1 = \frac{\pi(D_1^2 - D_0^2)}{4} p_1 + Q_m c_{01} \tag{7}$$

$$F_2 = \int_{r_1}^{r_2} p_{r2} \cdot 2\pi r dr \tag{8}$$

where D_0 is the diameter of impeller inlet hub, D_1 is the diameter of impeller inlet, p_1 is the inlet pressure of impeller, Q_m is the inlet mass flow rate, c_{01} is the inlet velocity,

Suppose that the change rule of p is as follows.

$$p_{r2} = p_1 + (p_2 - p_1) \left(\frac{r - r_1}{r_2 - r_1} \right)^2 \tag{9}$$

where p_2 is the outlet pressure of impeller, r_1 is the radius of impeller inlet, r_2 is the radius of impeller outlet.

The following relation is obtained:

$$F_2 = \int_{r_1}^{r_2} p_{r2} \cdot 2\pi r dr = \frac{\pi}{4} (D_2^2 - D_1^2) p_1 - \frac{8\pi(p_2 - p_1)}{(D_2 - D_1)^2} \left[\frac{D_2^4}{64} - \frac{D_1^4}{196} - \frac{D_2^3 D_1}{24} + \frac{D_2^2 D_1^2}{32} \right] \tag{10}$$

where D_2 is the diameter of impeller outlet.

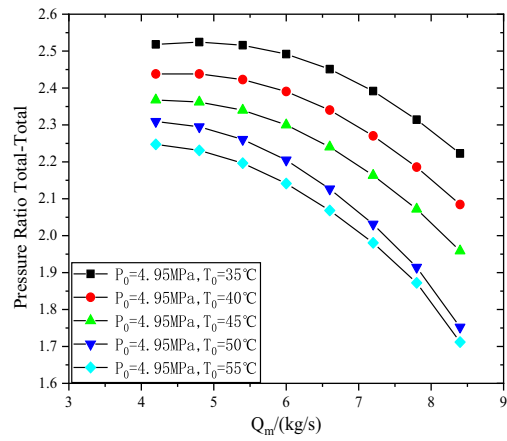
The axial thrust formula on the back of the impeller from the sealing diameter to the outer diameter of the impeller can be expressed as follows:

$$F_3 = 2\pi \int_{r_m}^{r_2} p_{r3} r dr = \frac{\pi}{4} (D_2^2 - d_m^2) p_2 - \frac{\pi \rho u_2^2}{32} \left((D_2^2 - d_m^2) - \frac{1}{2D_2^2} (D_2^4 - d_m^2) \right) \tag{11}$$

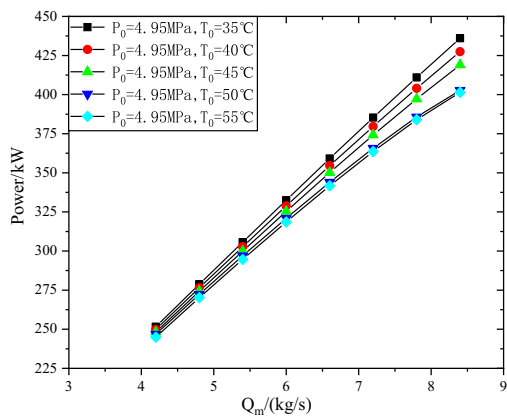
where d_m is the diameter of the sealing diameter between the back of the impeller and the motor.

The related dimension parameters of axial force are shown in Table 3.

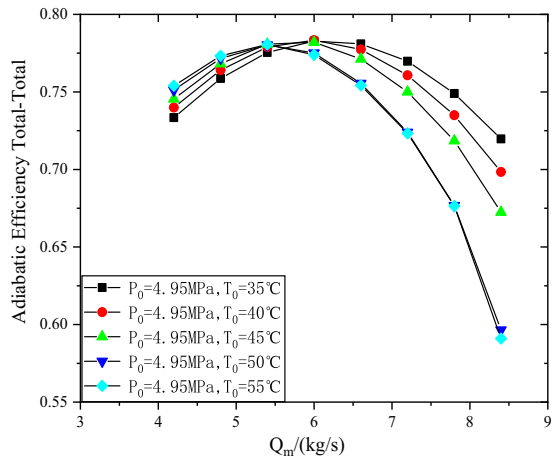
As shown in Fig. 10, the axial force of the first-stage impeller with different sealing diameters d_{m1} . With the increase of rotating speed, the axial force direction of the first-stage impeller changes from the reverse direction (inlet flow direction) to the positive direction. Due to the increase of rotating speed, the outlet pressure of the impeller increases and the gas force F_3 in Eq. (2) increases. With the increase of mass flow rate, the reverse value of axial force of the first-stage impeller increases and the positive value decreases, mainly because the gas force F_1 in Eq. (2) increases and the axial force value of the impeller decreases with the increase of mass flow rate. In the range of d_{m1} from 30 to 60 mm, with the increase of the diameter of the sealing diameter, the positive value of the axial force of the impeller decreases, the reverse value increases and the variation range of the axial force



(a) Pressure ratio total-total versus Q_m



(b) Power versus Q_m

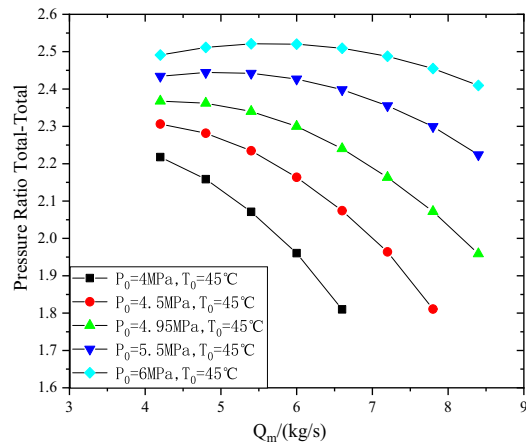


(c) Adiabatic efficiency total-total versus Q_m

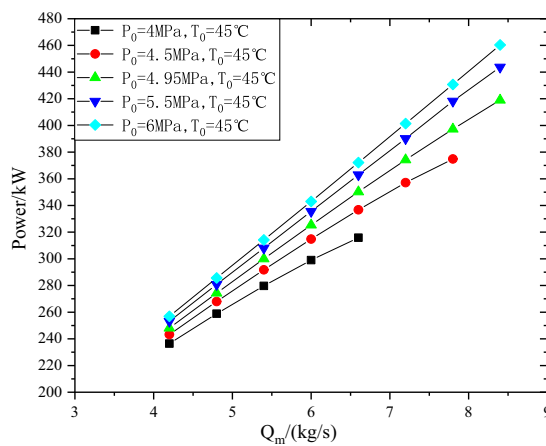
Figure 7. Performance curves of the compressor at 26000 rpm with different inlet temperatures.

decreases. In the range of rotating speed from 13000 to 26000 rpm, the axial force varies from -1.16kN to 8.51kN when sealing diameter d_{m1} is 30 mm, and from -12.14kN to -4.79kN when sealing diameter d_{m1} is 60 mm.

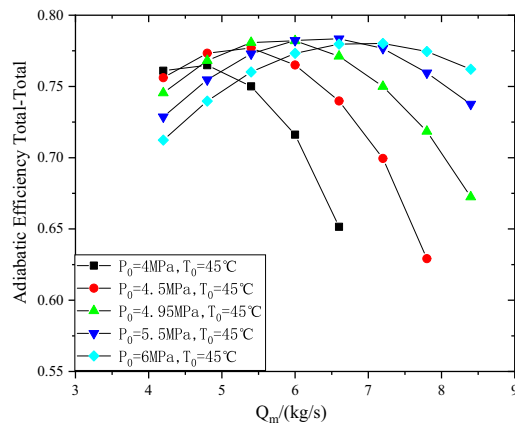
As shown in Fig. 11, the axial force of the second-stage impeller with different sealing diameters d_{m2} . The axial force variation law of the second-stage impeller is basically the same as that of the first-stage impeller. In the range of rotating speed from 13000 to 26000 rpm, when the sealing diameter d_{m2} is 30 mm, the axial force of the second-stage impeller changes from -2.36kN to 9.09kN , and when the sealing diameter d_{m2} is 60 mm,



(a) Pressure ratio total-total versus Q_m



(b) Power versus Q_m



(c) Adiabatic efficiency total-total versus Q_m

Figure 8. Performance curves of the compressor at 26000 rpm with different inlet pressures.

the axial force changes from -14.19kN to -11.63kN . When the sealing diameter d_{m2} is 60 mm, the axial force of the second-stage impeller has a smaller range than that of the first-stage impeller.

In the range of sealing diameter d_m from 30 to 60 mm, the axial force of compressor is shown in Fig. 12. When the first-stage impeller sealing diameter d_{m1} is constant, the positive value of the axial force of the compressor increases and the negative value decreases when the second-stage impeller sealing diameter d_{m2} ranges from 30 to 60 mm. When the sealing diameter of the second-stage impeller d_{m2} is constant, the positive value of the axial force of the compressor decreases and the negative value increases when the sealing diameter of the first-stage

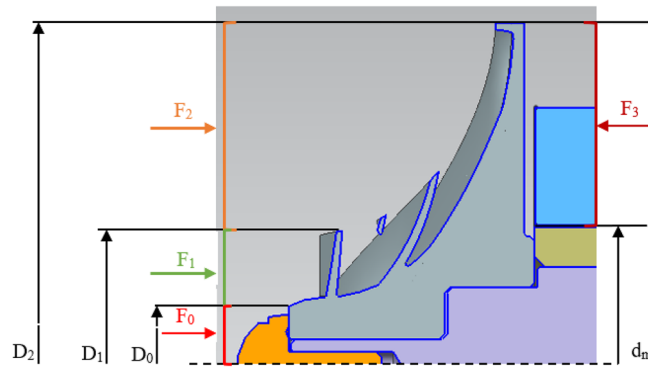


Figure 9. Axial force diagram of impeller.

	First stage	Second stage
D_0/mm	26	23.2
D_1/mm	52	46.4
D_2/mm	133	130.3

Table 3. Dimension parameters.

impeller d_{m1} ranges from 30 to 60 mm. Therefore, it is necessary to find two suitable sealing diameters d_{m1} and d_{m2} to keep the axial force of the compressor in a suitable fluctuation range and reduce the design difficulty of the thrust bearing.

Combined with the motor rotor size, and through the optimization of the first-stage seal diameter d_{m1} and the second-stage seal diameter d_{m2} , it is found that when $d_{m1} = 53.6$ mm and $d_{m2} = 47.2$ mm, the axial force of the compressor is within ± 1.5 kN, and the absolute value and variation range of the axial force are the best. The relationship between the axial force and the flow rate and speed is shown in Fig. 13.

A preliminary three-dimensional model of the compressor is shown in Fig. 14.

Rotor dynamics analysis

The rotor dynamics analysis of compressor rotor is completed by Dyrobes software. The rotor dynamics model is shown in Fig. 15. Shaft elements were used to model the rotor length, and diameter values of nuts, impellers, seal structure, thrust collar and motor rotor. Impellers can be modeled as disks. The mass, diametral moment of inertia and polar moment of inertia of the first-stage impeller are 1.01 kg, $7.198 \times 10^{-4} \text{m}^4$ and $1.328 \times 10^{-3} \text{m}^4$ respectively, and the mass, diametral moment of inertia and polar moment of inertia of the second-stage impeller are 0.88 kg, $6.095 \times 10^{-4} \text{m}^4$ and $1.139 \times 10^{-3} \text{m}^4$ respectively. Both radial bearing and thrust bearing adopt active magnetic bearing, and the initial values of stiffness and damping of radial bearing are set to 1000N/mm and 1N·s/mm respectively.

The critical speed map of the rotor is shown in Fig. 16. Due to the limitation of the stiffness of magnetic bearing, the critical speed will definitely appear in the operating speed range of carbon dioxide compressor in this study. Therefore, it is necessary to analyze the steady synchronous response of the rotor and further judge whether the compressor rotor is a rigid rotor according to the vibration mode of the rotor.

The goal of the rotor dynamics analysis was to study the forced unbalance response of rotor and evaluate the stability of the rotor³⁷. The rotor synchronous response at the first-order critical speed within the operating speed is shown in Fig. 17 and the results show that the vibration mode of the rotor is oscillating vibration mode and belongs to rigid vibration mode. Therefore, according to API Standard 617, the rotor is a rigid rotor.

When the radial bearing stiffness ranges from 1000N/mm to 7000N/mm, the lateral steady state response curves of rotor stations 1, 6, 16, 25 and 31 are shown in Fig. 18. With the increase of bearing stiffness, the first-order critical speed and maximum displacement of the rotor increase, and the amplification factor (AF) of each station also increases. And the results show that the first-order critical speed of the rotor is lower than the design speed. This is mainly because the stiffness adjustment range of magnetic bearing is limited (generally lower than $1 \times 10^4 \text{N/mm}$). As shown in Fig. 16, the first-order critical speed of the rotor cannot be greater than the design speed by adjusting the stiffness of magnetic bearing.

The lateral steady-state response curves of rotor stations 1, 6, 16, 25 and 31 with different diameters of motor rotor are shown in Fig. 19. When that diameter of the motor rotor is in the range of 60 mm to 120 mm, the maximum displacement of the rotor occurs at the position of Station 1. According to the rotor synchronous response in Fig. 17, the position of Station 1 is the maximum displacement under this vibration mode. With the increase of motor rotor diameter, the maximum displacement of the rotor increases. According to API Standard 617, with the increase of rotor diameter and rotor weight, the allowable unbalance value of the rotor increases, resulting in the increase of the maximum displacement of the rotor. When the motor rotor diameter is 120 mm,

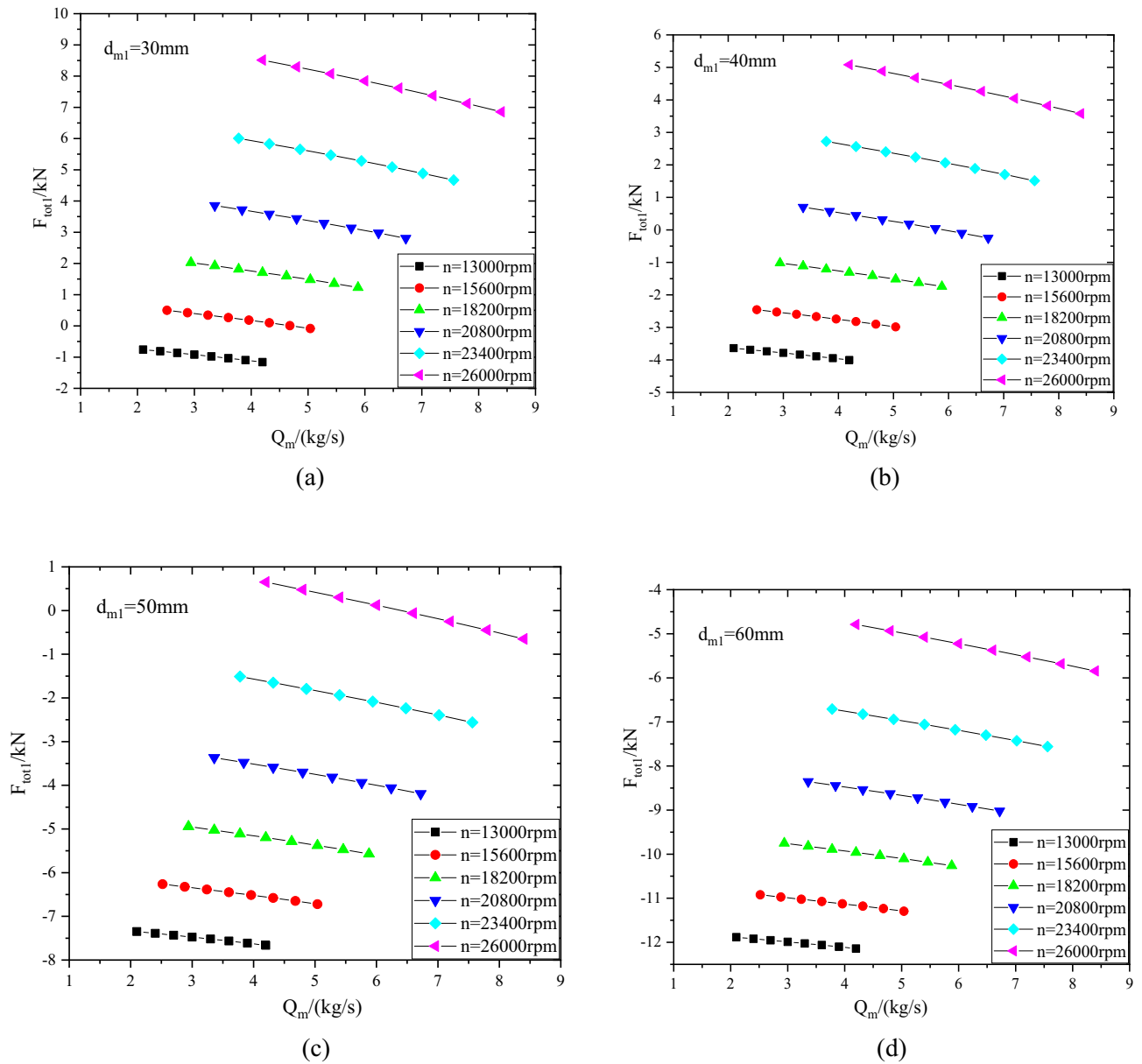


Figure 10. Axial force of first-stage impeller with different sealing diameters (a) $d_{m1} = 30\text{ mm}$, (b) $d_{m1} = 40\text{ mm}$, (c) $d_{m1} = 50\text{ mm}$, (d) $d_{m1} = 60\text{ mm}$.

the maximum displacement of the compressor rotor is 176.6% higher than that when the motor rotor diameter is 60 mm.

Results and discussion

In this paper, a centrifugal compressor in carbon dioxide heat pump system is designed. The compressor is directly driven by a high-speed permanent magnet synchronous motor. Two-stage impellers are installed on both sides of the motor, and the bearings are active magnetic bearings. The influences of inlet pressure and temperature on compressor performance are analyzed, the calculation method of compressor axial force is introduced, the axial force is calculated, analyzed and optimized, the rotor dynamics of compressor rotor is analyzed, and the influence of bearing stiffness on rotor dynamics is studied. The conclusions are summarized as follows.

(1) The density of carbon dioxide is greatly influenced by temperature and pressure. When the temperature is 45 °C and the pressure increases from 4 to 6 MPa, the density of carbon dioxide increases by 74.4%. The density of carbon dioxide increased by 20.5% when the pressure was 4.95 MPa and the temperature was increased from 30 to 60 °C.

In the range of inlet temperature from 35 to 55 °C, with the decrease of inlet temperature, the compressor pressure ratio increases by 12–29.8%, the power increases by 2.7–8.6%, and the efficiency decreases more slowly after the design point. In the range of inlet pressure from 4 to 6 MPa, with the increase of inlet pressure, the

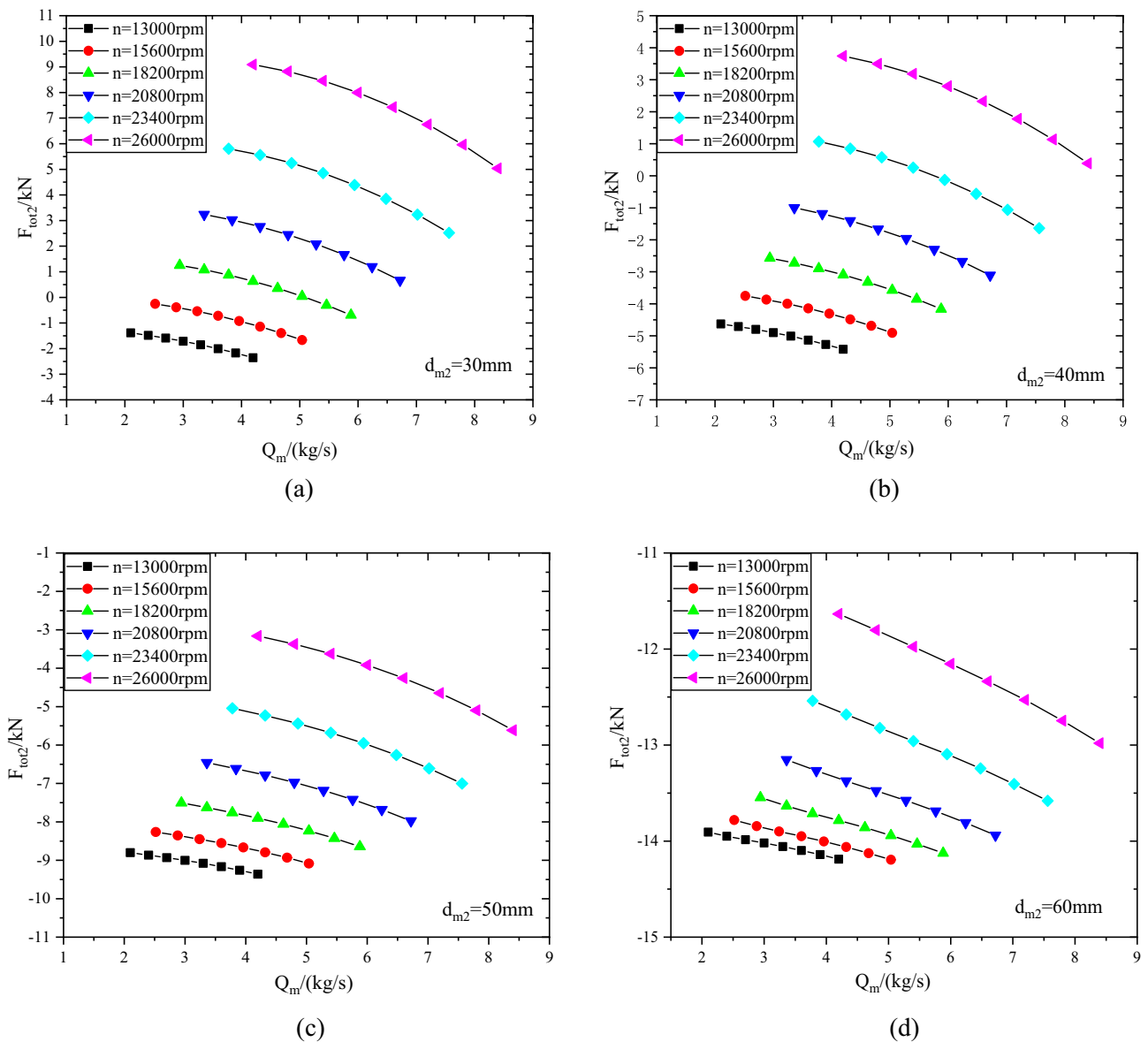


Figure 11. Axial force of second-stage impeller with different sealing diameters (a) $d_{m2} = 30$ mm, (b) $d_{m2} = 40$ mm, (c) $d_{m2} = 50$ mm, (d) $d_{m2} = 60$ mm.

compressor pressure ratio increases by 12.3–38.6%, and the power increases by 8.7–17.8%. The maximum inlet mass flow of compressor at inlet pressure of 4 MPa is 21.4% lower than that at inlet pressure of 6 MPa.

(2) With the increase of rotating speed, the axial force direction of the first-stage impeller changes from the reverse direction (inlet flow direction) to the positive direction. the axial force varies from -1.16 kN to 8.51 kN when sealing diameter d_{m1} is 30 mm, and from -12.14 kN to -4.79 kN when sealing diameter d_{m1} is 60 mm. When the first-stage impeller sealing diameter d_{m1} is constant, the positive value of the axial force of the compressor increases and the negative value decreases when the second-stage impeller sealing diameter d_{m2} ranges from 30 to 60 mm. Through the optimization of the first-stage seal diameter d_{m1} and the second-stage seal diameter d_{m2} , it is found that when $d_{m1} = 53.6$ mm and $d_{m2} = 47.2$ mm, the absolute value and variation range of the axial force of the compressor are the best.

(3) The vibration mode of the rotor is oscillating vibration mode and the rotor is a rigid rotor. With the increase of bearing stiffness, the first-order critical speed and maximum displacement of the rotor increase, and the amplification factor (AF) of each station also increases. When the motor rotor diameter is 120 mm, the maximum displacement of the compressor rotor is 176.6% higher than that when the motor rotor diameter is 60 mm.

The analysis results in this paper can provide reference for the design of centrifugal compressor in carbon dioxide heat pump system. In the future research work, it is necessary to test and verify the design and analysis results and increase the design power of carbon dioxide heat pump system and centrifugal compressor to ensure their wider popularization and use.

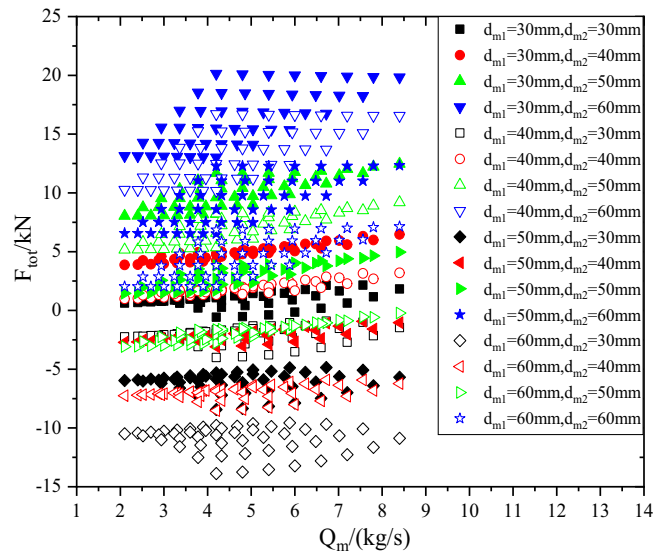


Figure 12. Axial force of compressor.

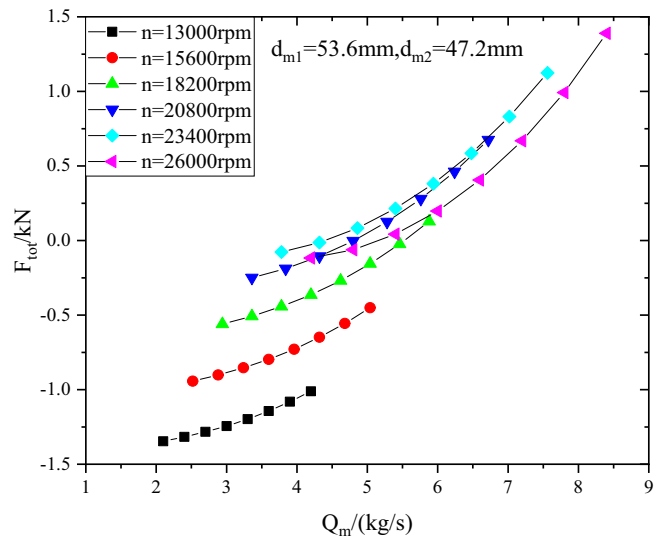
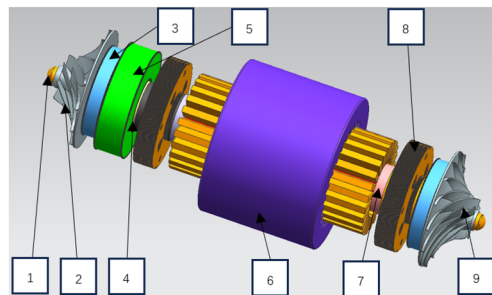
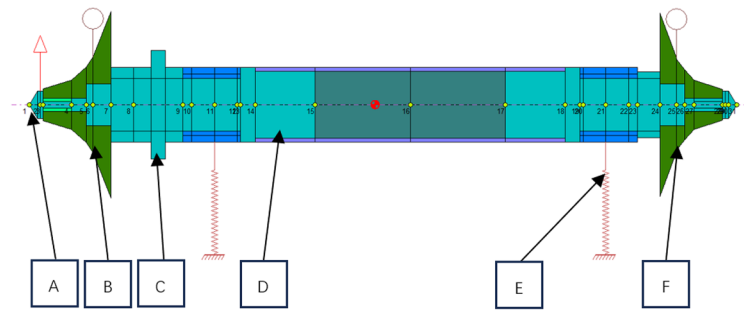


Figure 13. Axial force of compressor when $d_{m1} = 53.6$ mm and $d_{m2} = 47.2$ mm.



(1) Nut, (2) First Stage Impeller, (3) Seal Structure, (4) Thrust Collar, (5) Thrust Bearing, (6) Motor Stator, (7) Motor Rotor, (8) Radial Bearing, (9) Second Stage Impeller

Figure 14. Preliminary three-dimensional model of the compressor.



A. Nut, B. First Stage Impeller, C. Thrust Collar, D. Motor Rotor, E. Radial Bearing, F. Second Stage Impeller

Figure 15. Rotor dynamics model of compressor. A.

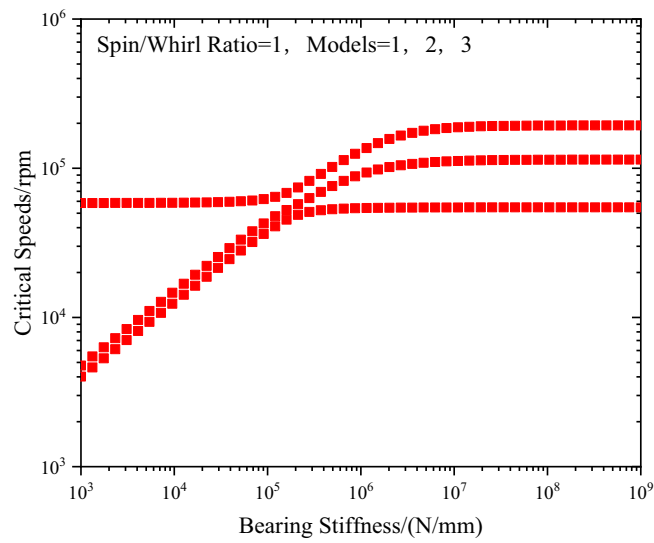


Figure 16. Critical speed map.

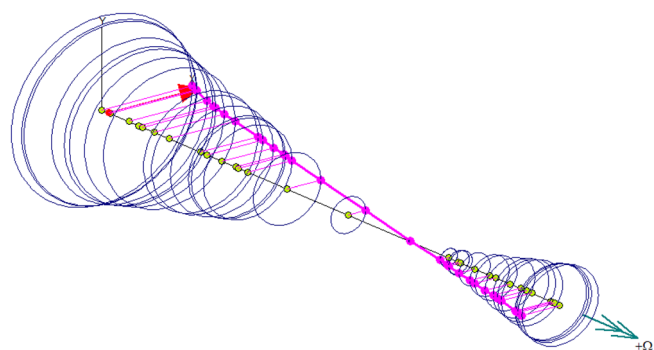


Figure 17. Rotor synchronous response.

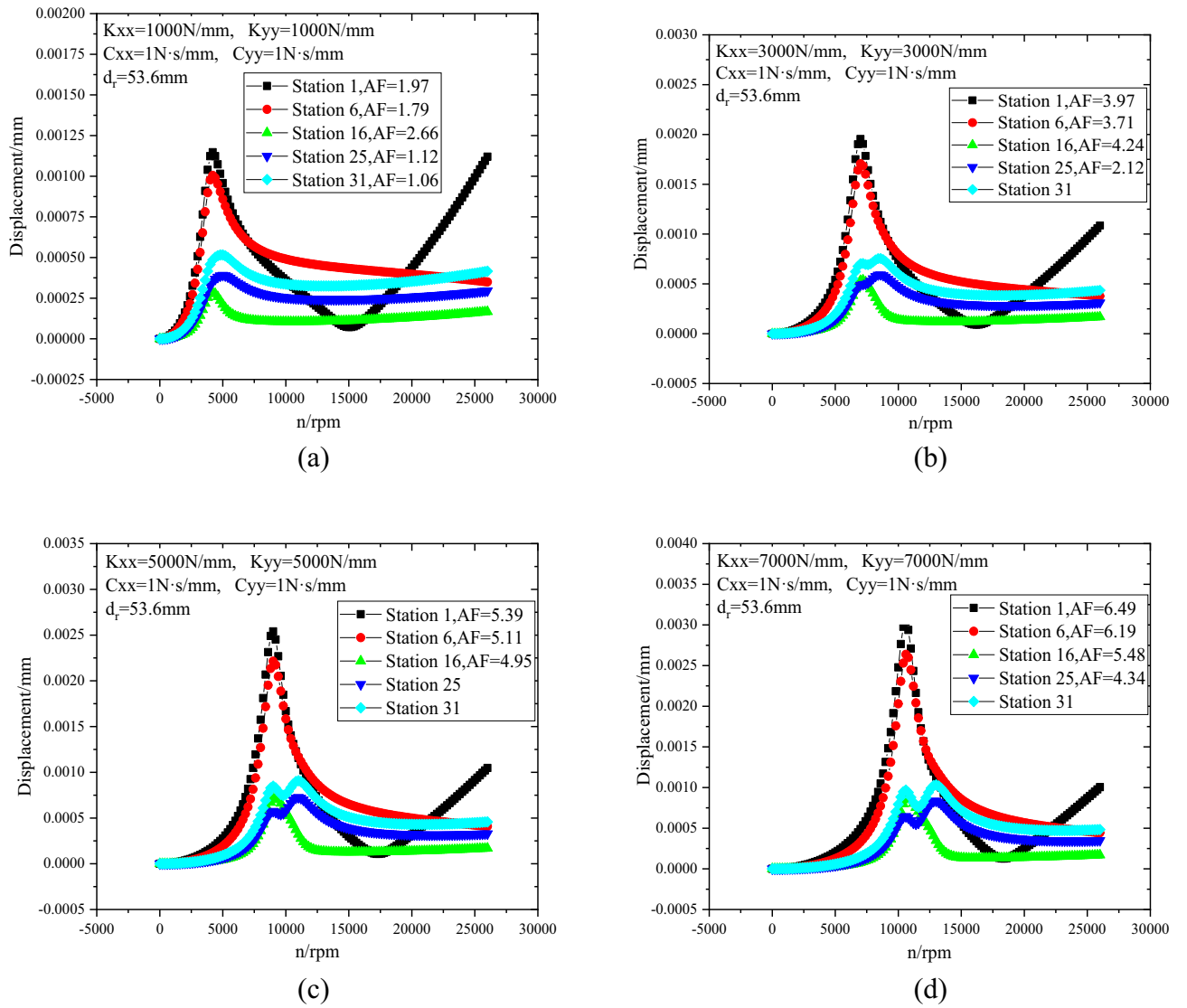


Figure 18. Lateral steady state response with different radial bearing stiffness (a) $K_{xx} = K_{yy} = 1000 \text{ mm}$, (b) $K_{xx} = K_{yy} = 3000 \text{ mm}$, (c) $K_{xx} = K_{yy} = 5000 \text{ mm}$, (d) $K_{xx} = K_{yy} = 7000 \text{ mm}$.

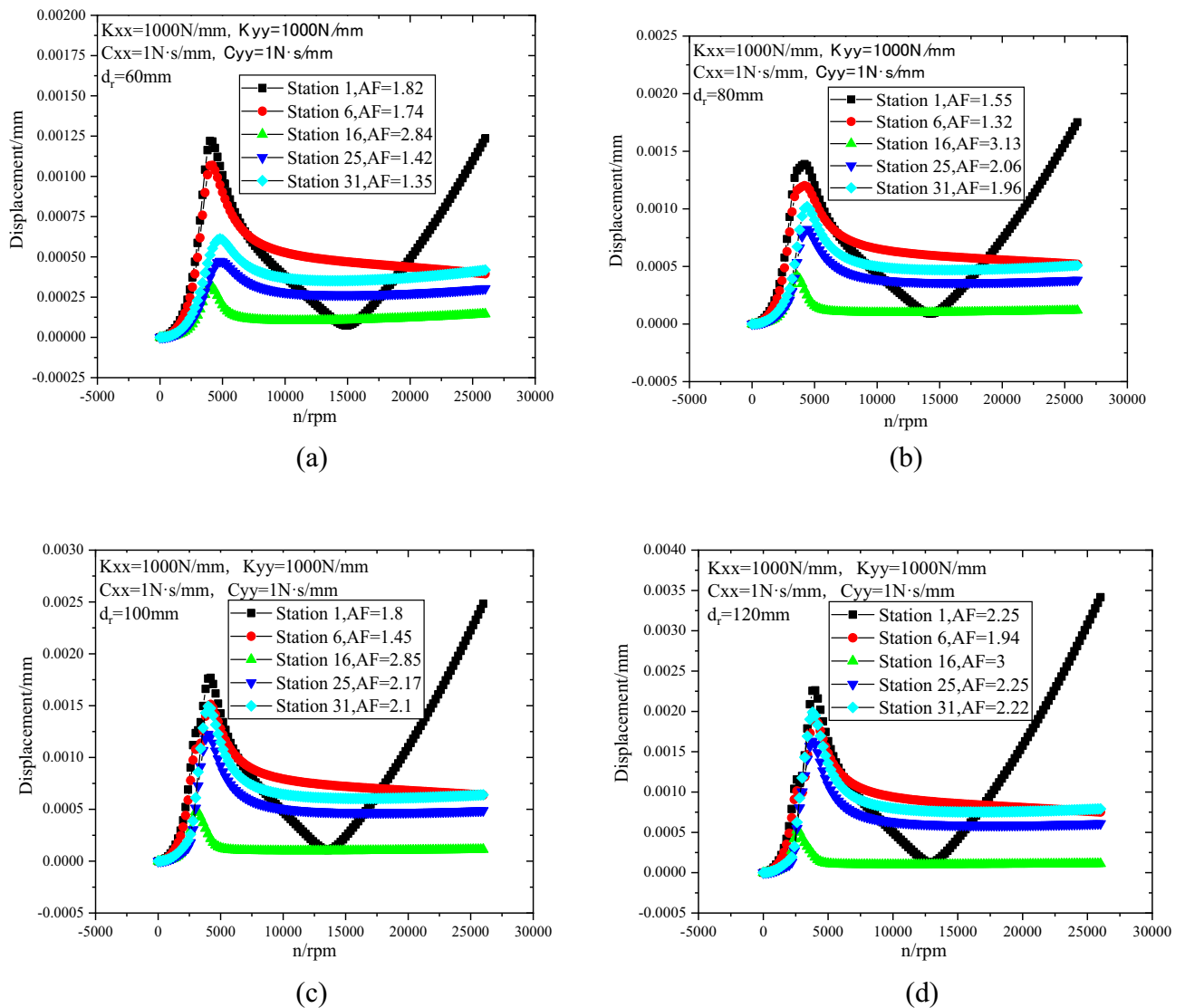


Figure 19. Lateral steady state response with different diameters of motor rotor (a) $d_r=60\text{ mm}$, (b) $d_r=80\text{ mm}$, (c) $d_r=100\text{ mm}$, (d) $d_r=120\text{ mm}$.

Data availability

The datasets generated and/or analysed during the current study are not publicly available due to requirement of confidentiality, but are available from the corresponding author on reasonable request.

Received: 20 December 2023; Accepted: 27 February 2024

Published online: 04 March 2024

References

- Mohtasham, J. Review article-renewable energies. *Energy Proc.* **74**, 1289–1297 (2015).
- Dogaru, L. The main goals of the fourth industrial revolution, renewable energy perspectives. *Proc. Manuf.* **46**, 397–401 (2020).
- Naterer, G. F., Dincer, I. & Zamfirescu, C. *Hydrogen Production from Nuclear Energy* (Springer, 2013).
- Graves, C., Ebbesen, S. D., Mogensen, M. & Lackner, K. S. Sustainable hydrocarbon fuels by recycling CO_2 and H_2O with renewable or nuclear energy. *Renew. Sustain. Energy Rev.* **15**, 1–23 (2011).
- Kannan, N. & Vakeesan, D. Solar energy for future world: - A review. *Renew. Sustain. Energy Rev.* **62**, 1092–1105 (2016).
- Hosseini, S. E. & Wahid, M. A. Hydrogen from solar energy, a clean energy carrier from a sustainable source of energy. *Int. J. Energy Res.* **44**(6), 4110–4131 (2020).
- Roga, S., Bardhan, S., Kumar, Y. & Dubey, S. K. Recent technology and challenges of wind energy generation: A review. *Sustain. Energy Techn.* **52**(1), 102239 (2022).
- Olabi, A. G. *et al.* Selection guidelines for wind energy technologies. *Energies* **14**, 3244. <https://doi.org/10.3390/en14113244> (2021).
- Bildirici, M. E. Economic growth and biomass energy. *Biomass Bioenergy* **50**, 19–24 (2013).
- Rosillo-Calle, F. A review of biomass energy - shortcomings and concerns. *J. Chem. Technol. Biotechnol.* **91**(7), 1933–1945 (2016).
- Rosen, M. A. & Koohi-Fayegh, S. The prospects for hydrogen as an energy carrier: An overview of hydrogen energy and hydrogen energy systems. *Energy Ecol. Environ.* **1**, 10–29 (2016).

12. Abe, J. O., Popoola, A. P. I., Ajenifuja, E. & Popoola, O. M. Hydrogen energy, economy and storage: Review and recommendation. *Int. J. Hydrogen Energy* **44**(29), 15072–15086 (2019).
13. Lund, J. W. & Toth, A. N. Direct utilization of geothermal energy 2020 worldwide review. *Geothermics* **90**, 101915 (2021).
14. Chowdhury, M. S. *et al.* Current trends and prospects of tidal energy technology. *Environ. Dev. Sustain.* **23**, 8179–8194 (2021).
15. Chaichana, C., Aye, L. & Charters, W. W. S. Natural working fluids for solar-boosted heat pumps. *Int. J. Refrig.* **26**(6), 637–643 (2003).
16. Wang, J. *et al.* A comprehensive review and analysis on CO₂ heat pump water heaters. *Energy Convers. Manag.* **X 15**, 100277. <https://doi.org/10.1016/j.ecmx.2022.100277> (2022).
17. Zhang, J.-F., Qin, Y. & Wang, C.-C. Review on CO₂ heat pump water heater for residential use in Japan. *Renew. Sustain. Energy Rev.* **50**, 1383–1391 (2015).
18. Yingjie, Xu. *et al.* Optimization on integrated inverter-compressor CO₂ heat pump with new operating model. *Appl. Therm. Eng.* **200**, 117632 (2022).
19. Nawaz, K., Shen, Bo., Elatar, A., Baxter, V. & Abdelaziz, O. Performance optimization of CO₂ heat pump water heater. *Int. J. Refrig.* **85**, 213–228 (2018).
20. Tafur-Escant, P., Valencia-Chapi, R., López-Guillem, M., Fierros-Peraza, O. & Muñoz-Antón, J. Electrical energy storage using a supercritical CO₂ heat pump. *Energy Rep.* **8**, 502–507 (2022).
21. Qin, X., Zhang, Y., Wang, D. & Chen, J. System development and simulation investigation on a novel compression/ejection trans-critical CO₂ heat pump system for simultaneous cooling and heating. *Energy Convers. Manag.* **259**, 115579 (2022).
22. Wang, Y., Ye, Z., Song, Y., Yin, X. & Cao, F. Experimental investigation on the hot gas bypass defrosting in air source transcritical CO₂ heat pump water heater. *Appl. Therm. Eng.* **178**, 115571 (2020).
23. Ibsaine, R., Joffroy, J.-M. & Stouffs, P. Modelling of a new thermal compressor for supercritical CO₂ heat pump. *Energy* **117**, 530–539 (2016).
24. Yang, B., Bradshaw, C. R. & Groll, E. A. Modeling of a semi-hermetic CO₂ reciprocating compressor including lubrication sub-models for piston rings and bearings. *Int. J. Refrig.* **36**, 1925–1937 (2013).
25. Zheng, S. *et al.* Impact of micro-grooves in scroll wrap tips on the performance of a trans-critical CO₂ scroll compressor. *Int. J. Refrig.* **131**, 493–504 (2021).
26. Zheng, S., Mingshan Wei, Yu., Zhou, C. H. & Song, P. Tangential leakage flow control with seal-grooves on the static scroll of a CO₂ scroll compressor. *Appl. Therm. Eng.* **208**, 118213 (2022).
27. Stosic, N., Smith, I. K. & Kovacevic, A. A twin screw, combined compressor and expander for CO₂ refrigeration systems. In *International Compressor Engineering Conference*, p. 1591 (2002).
28. Meroni, A., Zühlsdorf, B., Elmegaard, B. & Haglind, F. Design of centrifugal compressors for heat pump systems. *Appl. Energy* **232**, 139–156 (2018).
29. Cao, R., Deng, Q., Li, Z., Li, J. & Gao, T. Design strategy for inlet conditions of supercritical CO₂ centrifugal compressors. *J. Supercrit. Fluids* **196**, 105879 (2023).
30. Park, J. H., Cha, J. E. & Lee, S. W. Experimental investigation on performance test of 150-kW-class supercritical CO₂ centrifugal compressor. *Appl. Therm. Eng.* **210**, 118310 (2022).
31. Hosseinpour, J., Messele, M. & Engeda, A. Analysis and design of centrifugal compressor for 10 MWe supercritical CO₂ Brayton cycles. *J. Mech. Sci. Technol.* **37**(5), 2607–2621 (2023).
32. Pengcheng, Xu., Zou, Z. & Chao, Fu. Aerodynamic design considerations for supercritical CO₂ centrifugal compressor with real-gas effects. *Energy Convers. Manag.* **271**, 116318 (2022).
33. Xia, W., Zhang, Y., Yu, H., Han, Z. & Dai, Y. Aerodynamic design and multi-dimensional performance optimization of supercritical CO₂ centrifugal compressor. *Energy Convers. Manag.* **248**, 114810 (2021).
34. API Standard 617. Axial and Centrifugal Compressors and Expander-Compressors for Petroleum, Chemical and Gas Industry Services, Washington, D.C.: American Petroleum Institute (2002).
35. Concepts NREC, 2015. [Online]. Available: <http://www.conceptsnrec.com/>.
36. Hang, Z., Wang, X. & Wang, W. *Turbine Compressor* 112–150 (Chemical Industry Press, 2013).
37. Jiang, P., Wang, Bo., Tian, Y., Xu, X. & Zhao, L. Design of a supercritical CO₂ compressor for use in a 1 MWe power cycle. *ACS Omega* **6**, 33769–33778 (2021).

Acknowledgements

The authors are grateful to the National Natural Science Foundation of China (Grant No.: 52006216 and No.: 52176090) and CAS Project for Young Scientists in Basic Research (Grant No.: YSBR-043) for the financial assistance for this study.

Author contributions

P.J. and Y.T. wrote the main manuscript text. B.W. prepared Figures 1, 2, 3, 4, 5, 6, 7, 8, 9, 10, 11 and 12. C.G. prepared Figures 15, 16, 17, 18 and 19. All authors reviewed the manuscript.

Competing interests

The authors declare no competing interests.

Additional information

Correspondence and requests for materials should be addressed to P.J.

Reprints and permissions information is available at www.nature.com/reprints.

Publisher's note Springer Nature remains neutral with regard to jurisdictional claims in published maps and institutional affiliations.



Open Access This article is licensed under a Creative Commons Attribution 4.0 International License, which permits use, sharing, adaptation, distribution and reproduction in any medium or format, as long as you give appropriate credit to the original author(s) and the source, provide a link to the Creative Commons licence, and indicate if changes were made. The images or other third party material in this article are included in the article's Creative Commons licence, unless indicated otherwise in a credit line to the material. If material is not included in the article's Creative Commons licence and your intended use is not permitted by statutory regulation or exceeds the permitted use, you will need to obtain permission directly from the copyright holder. To view a copy of this licence, visit <http://creativecommons.org/licenses/by/4.0/>.

© The Author(s) 2024